Computers and Structures 199 (2018) 1–17

Contents lists available at ScienceDirect

Computers and Structures

journal homepage: www.elsevier.com/locate/compstruc

The new paradigm of finite element solutions with overlapping elements in CAD – Computational efficiency of the procedure

Lingbo Zhang, Ki-Tae Kim, Klaus-Jürgen Bathe *

Massachusetts Institute of Technology, Cambridge, MA 02139, USA

ARTICLE INFO

Article history:
Received 10 October 2017
Accepted 7 January 2018

Keywords:
Finite elements
Overlapping finite elements
CAD & CAE
Geometry clean-up
Meshing
Computational efficiency

ABSTRACT

We consider the new paradigm of finite element analysis, present an effective overlapping finite element, and study the computational efficiency of the discretization scheme.

The important new ingredient in the formulation of the overlapping element is that, unlike in meshless methods, we only use local polynomial functions in the displacement interpolations. We achieve this property by replacing the Shepard functions by local polynomials. As a consequence, the bandwidth of the resulting stiffness matrix for the overlapping finite element is much reduced when compared with earlier developments.

We study the distortion insensitivity of the new overlapping finite element, the convergence properties and the required computational effort when compared with the use of the traditional 4-node finite element and that element with covers. The results show the overlapping element to be very promising, in particular in the new paradigm of analysis using finite elements in CAD.

1. Introduction

The computational procedures and resources available today make the finite element analysis of complex structures and fluid systems possible. However, due to meshing difficulties, significant experience in building effective meshes is still needed. In practice, much more time may be spent by an engineer to reach an adequate mesh than the time used by the finite element program for the calculation and solution of the governing equations. Indeed, it is well-known that the experience and time required for an analysis impedes the wider use of finite element analysis in the field of computer-aided design (CAD).

To overcome the meshing difficulties, a number of unstructured mesh generation algorithms have been proposed, see e.g. Refs. [1–3]. The goal is to develop a robust and efficient mesh generator that automatically builds high-quality finite element meshes for large and complex geometries. Since the data defining the geometry is frequently not directly usable, the engineer usually has to first clean up the geometry [4]. Then in order to reach an adequate mesh, a considerable amount of engineering time and computational effort may be required [3]. Also, an unstructured mesh generator may perform quite well for simple geometries but may fail in building an adequate mesh for geometrically complex objects.

For these reasons, many meshfree or meshless methods have been proposed, see e.g. Ref. [5]. However, while using a meshfree method the time to establish the discretization is much less and good solution accuracy can be obtained, the method may not be stable unless artificial stability parameters are used, or the required numerical integration may be computationally very expensive, and inherently so, see e.g. Refs. [5–9] and the references therein. These limitations largely restrict the wide use of meshfree methods in engineering practice.

To significantly reduce the meshing effort required in finite element analysis, we proposed a new paradigm of finite element solutions in computer-aided design [10–12]. In the new paradigm, the geometry is obtained from any CAD program or by any other means. Hence the procedure is not limited, for example, to dealing only with geometries represented by NURBS. The geometry is immersed in a Cartesian grid of (usually uniform) cells, the boundary of the geometry is discretized while defects are removed, and cells within the analysis domain are automatically, and with little computational effort, converted to traditional finite elements. Thereafter, overlapping finite elements are inserted to fill-in the empty space and couple with the traditional finite elements. The solution accuracy is good because undistorted traditional finite elements [13,14] and distortion insensitive overlapping finite elements are used [12]. Moreover, since the analysis domain is largely meshed with uniform finite elements, a stress improvement procedure can be used effectively [15].

* Corresponding author.
E-mail address: kjb@mit.edu (K.J. Bathe).

https://doi.org/10.1016/j.compstruc.2018.01.003
0045-7949/

This approach is clearly related to schemes using "overlapping grids" in finite difference and control volume solutions of fluid flows, see e.g. Refs. [16–20]. Here finite difference grids are superimposed to cover the complete analysis domain. While our approach for finite element analysis is related to these schemes, it shows much more generality.

In our previous papers, we proposed the general procedure of the new paradigm of solutions, the coupling scheme between overlapping elements and traditional finite elements, and a new overlapping element that is distortion insensitive and not expensive in the numerical integration. However, the overlapping element leads to a much larger bandwidth than the traditional finite elements.

In this paper, we focus on a significant improvement of the overlapping element of Ref. [12] and evaluate the computational efficiency of the new paradigm of solutions when using this element. First, in Section 2 we present the formulation of the improved overlapping element, which gives a much smaller bandwidth than the element in Ref. [12], and we discuss the required numerical integration and the element insensitivity to geometric distortions. Then in Section 3, we study the computational efficiency of the new overlapping element; namely in the required numerical integration and in the solution of the equations in comparison to using the traditional 4-node finite elements. We also study the convergence properties of the overlapping finite element. Thereafter, in Section 4, we illustrate the complete analysis approach of the new paradigm in the analysis

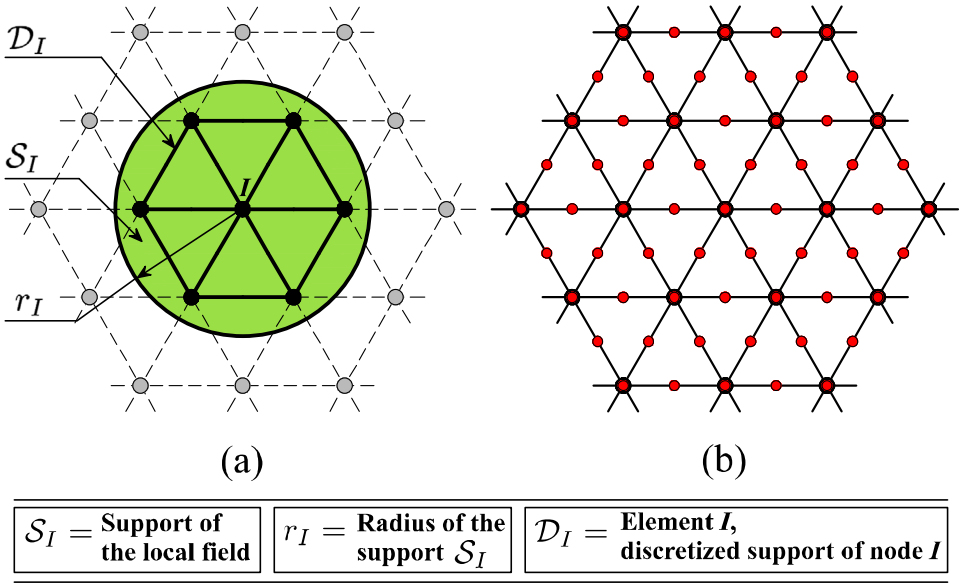

Fig. 1. Schematic of the new overlapping element with triangular overlap regions; (a) the 7-node overlapping element $\mathcal{D}_I$; (b) the mesh of the overlapping elements with red virtual nodes included. (To see the colors in this figure and all subsequent figures, refer to the web version of the paper.)

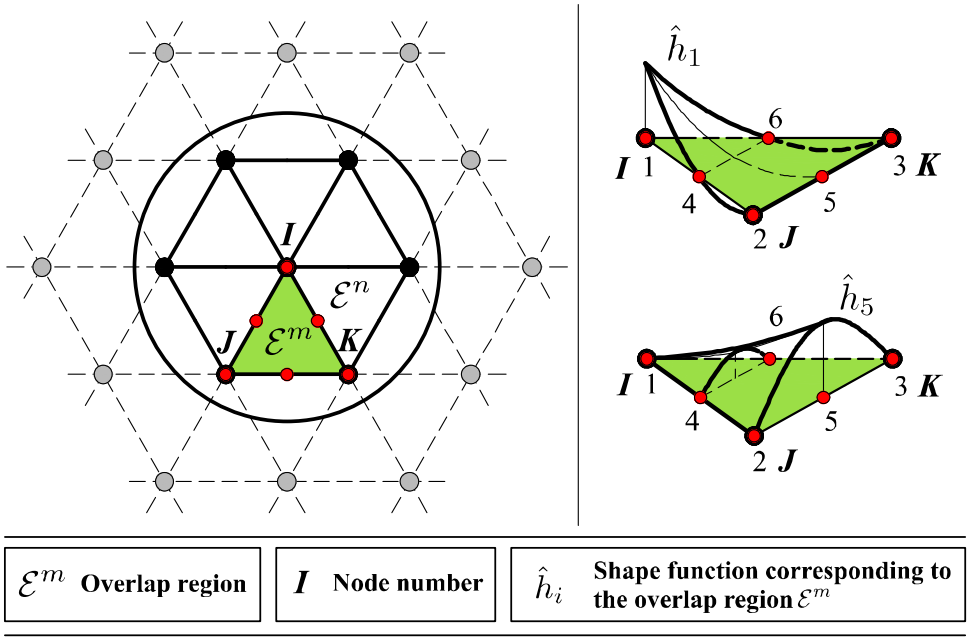

Fig. 2. Schematic of shape functions $\hat{h}_1$, $\hat{h}_5$ corresponding to the overlap region $\mathcal{E}^m$; there are 6 virtual nodes for $\mathcal{E}^m$, numbered from 1 to 6.

Table 1
Interpolation functions $\hat{\varphi}_I^I(\mathbf{x})$, $\hat{\varphi}_J^I(\mathbf{x})$ and $\hat{\varphi}_K^I(\mathbf{x})$ of the overlapping element $\mathcal{D}_I$ in the overlap region $\mathcal{E}^m$ corresponding to the nodes I, J, K that contribute.

$\hat{\varphi}_I^I(\mathbf{x}) = \sum_{i=1}^{6} \hat{h}_i \hat{\varphi}_{Ii}^I$					
$\hat{\varphi}_{I1}^I$	$\hat{\varphi}_{I2}^I$	$\hat{\varphi}_{I3}^I$	$\hat{\varphi}_{I4}^I$	$\hat{\varphi}_{I5}^I$	$\hat{\varphi}_{I6}^I$
1	0	0	$\left.\frac{W_I}{W_I+W_J}\right\|_{\mathbf{x}_4}$	$\left.\frac{W_I}{W_I+W_J+W_K}\right\|_{\mathbf{x}_5}$	$\left.\frac{W_I}{W_I+W_K}\right\|_{\mathbf{x}_6}$
$\hat{\varphi}_J^I(\mathbf{x}) = \sum_{i=1}^{6} \hat{h}_i \hat{\varphi}_{Ji}^I$					
$\hat{\varphi}_{J1}^I$	$\hat{\varphi}_{J2}^I$	$\hat{\varphi}_{J3}^I$	$\hat{\varphi}_{J4}^I$	$\hat{\varphi}_{J5}^I$	$\hat{\varphi}_{J6}^I$
0	1	0	$\left.\frac{W_J}{W_I+W_J}\right\|_{\mathbf{x}_4}$	$\left.\frac{W_J}{W_I+W_J+W_K}\right\|_{\mathbf{x}_5}$	0
$\hat{\varphi}_K^I(\mathbf{x}) = \sum_{i=1}^{6} \hat{h}_i \hat{\varphi}_{Ki}^I$					
$\hat{\varphi}_{K1}^I$	$\hat{\varphi}_{K2}^I$	$\hat{\varphi}_{K3}^I$	$\hat{\varphi}_{K4}^I$	$\hat{\varphi}_{K5}^I$	$\hat{\varphi}_{K6}^I$
0	0	1	0	$\left.\frac{W_K}{W_I+W_J+W_K}\right\|_{\mathbf{x}_5}$	$\left.\frac{W_K}{W_I+W_K}\right\|_{\mathbf{x}_6}$

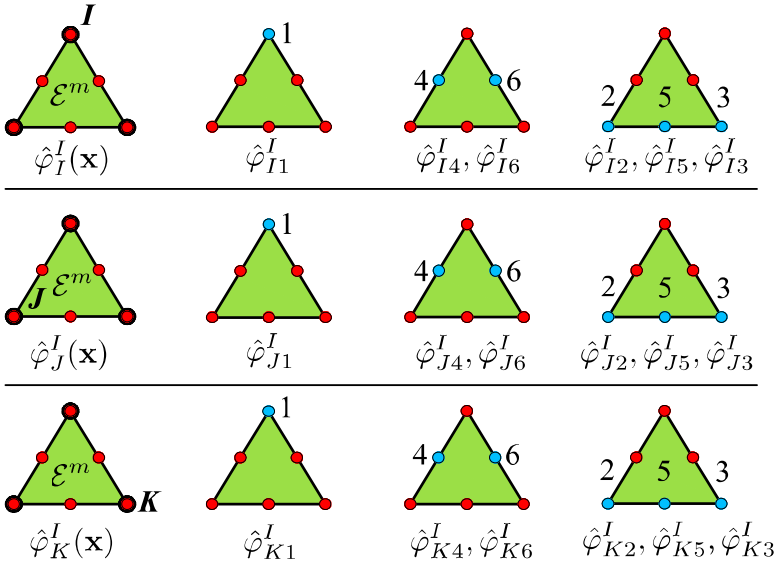

Fig. 3. Schematic indicating nodal values that are used for the interpolation functions $\hat{\varphi}_I^I(\mathbf{x})$, $\hat{\varphi}_J^I(\mathbf{x})$ and $\hat{\varphi}_K^I(\mathbf{x})$, in the overlap region $\mathcal{E}^m$; the blue nodes denote the virtual nodes corresponding to the listed nodal values.

of a cantilever plate with holes, and in Section 5 we give briefly some remarks regarding the solution of three-dimensional problems. Finally, we present our conclusions in Section 6.

2. The new overlapping finite element

Our objective in this section is to propose a significant improvement on the overlapping finite element given in Ref. [12]. We use no longer rational functions in the element formulation and, most importantly, the bandwidth of the stiffness matrix is much reduced.

2.1. Discretization using the new overlapping element

The new overlapping element is formulated quite similarly to the element in Ref. [12]. The local analysis domain $\mathcal{D}_I$ in Fig. 1, given by the union of the 6 triangular "overlap regions" (or "regions of overlap"), denotes the discretized support of node I, and we refer to it as element I.

In order to reduce the bandwidth, virtual nodes (see the red nodes in Fig. 1(b)) are automatically generated on the physical nodes and at the middle of the sides of the triangles. The virtual nodes are not real nodes since no degrees of freedom are assigned and they are only used to establish the local field of the solution approximation. These fields are then used to obtain the global approximation.

2.2. Local interpolation

Let $\mathcal{N}_I$ be the set of nodes contained in $\mathcal{D}_I$

$$\mathcal{N}_I := \{M : \mathcal{D}_M \cap \mathcal{D}_I \neq \varnothing\} \tag{1}$$

where M denotes a node number. Consider a sphere $\mathcal{S}_I$ with center at node I and containing all nodes in $\mathcal{N}_I$.

In the overlapping finite element of Ref. [12] the local field in the domain $\mathcal{S}_I$ is assumed to be

$$\boldsymbol{\psi}_I(\mathbf{x}) = \sum_{J\in\mathcal{N}_I}\sum_{n\in\mathfrak{I}} \varphi_J^I(\mathbf{x})(p_n \mathbf{a}_{Jn}) \tag{2}$$

with the Shepard function $\varphi_J^I(\mathbf{x})$ given as

$$\varphi_J^I(\mathbf{x}) = \frac{W_J^I(\mathbf{x})}{\sum_{K\in\mathcal{N}_I} W_K^I(\mathbf{x})} \tag{3}$$

where $W_J^I(\mathbf{x})$ is the weight function of node J in the overlapping element $\mathcal{D}_I$. In Eq. (2), p_n denotes the nth polynomial term corresponding to node J in

$$\mathbf{p}^T = [1 \quad x \quad y \quad x^2 \quad xy \quad \cdots] \tag{4}$$

Here, the coordinate variables (x, y) are measured from node J, with the origin of the coordinate system located at node J. In Eq. (2), $\mathbf{a}_{Jn} = [a_{Jn}^u \; a_{Jn}^v]$ represents the unknown nodal variables. While we refer in our description largely to a single overlapping element, the formulation can thus also be interpreted to be for a family of elements, because different basis functions can be used in Eq. (4).

We illustrated in Ref. [12] that for the proposed overlapping element, numerical integration using 9 points in each overlap region is sufficient (despite the use of the rational function in Eq. (3)). However, the bandwidth of the stiffness matrix is relatively large because all nodes contained in $\mathcal{N}_I$ are used. In order to reduce the bandwidth and interpolate the displacement field with polynomials, we now replace the Shepard functions by quadratic interpolations.

Specifically, using the virtual nodes, we define in every overlap region an interpolation function $\hat{\varphi}_J^I(\mathbf{x})$ that we use instead of the function $\varphi_J^I(\mathbf{x})$:

$$\hat{\varphi}_J^I(\mathbf{x}) = \sum_{i=1}^{6} \hat{h}_i \hat{\varphi}_{Ji}^I \tag{5}$$

where $\hat{h}_i$ is the usual shape function of second order two-dimensional elements used in finite element analysis [14], and $\hat{\varphi}_{Ji}^I$ is the nodal value (obtained from the Shepard function) of the virtual node i. The local field in the domain $\mathcal{S}_I$ is then given as

$$\boldsymbol{\psi}_I(\mathbf{x}) = \sum_{J\in\mathcal{N}_I}\sum_{n\in\mathfrak{Z}} \hat{\varphi}_J^I(\mathbf{x})(p_n \mathbf{a}_{Jn}) = \sum_{J\in\mathcal{N}_I}\left(\sum_{i=1}^{6} \hat{h}_i \hat{\varphi}_{Ji}^I \sum_{n\in\mathfrak{Z}} (p_n \mathbf{a}_{Jn})\right) \tag{6}$$

We shall use this local field to construct the global field with the contribution of $h_I\boldsymbol{\psi}_I$ where h_I is the standard 3-node element displacement interpolation function, which is zero on the side J-K of the overlap region shown in Fig. 2. The additional contributions arise from the elements J and K, that is, the discretized supports of nodes J and K (see Section 2.3).

Accordingly, the function $\hat{\varphi}_J^I(\mathbf{x})$ is built to satisfy three criteria:

Criterion I. In order to reduce the bandwidth, the local field $\boldsymbol{\psi}_I(\mathbf{x})$ in every overlap region is only defined using the physical nodes of that region. For example, in Fig. 2, the local field $\boldsymbol{\psi}_I(\mathbf{x})$ in the overlap region $\mathcal{E}^m$ is only defined by the values at the nodes I, J, K.

Criterion II. The function $\hat{\varphi}_J^I(\mathbf{x})$ must be continuous in the overlapping element $\mathcal{D}_I$. For example in Fig. 2, continuity requires that the values of the functions corresponding to $\mathcal{E}^m$ and $\mathcal{E}^n$ on the edge I-K are defined only by virtual nodes on that line (like continuity is established in usual finite element analysis [14]).

Criterion III. The function $\hat{\varphi}_J^I(\mathbf{x})$ is greater than or equal to 0 at the six virtual nodes, and the functions $\hat{\varphi}_J^I(\mathbf{x})$ satisfy the partition of unity: $\sum_{J=1}^{\mathcal{N}_I} \hat{\varphi}_J^I(\mathbf{x}) = 1$, with $\hat{\varphi}_J^I(\mathbf{x}_J) = 1$, for $J \in \mathcal{N}_I$.

Based on the above criteria, we use that for the nodal values $\hat{\varphi}_{Ji}^I$ in each overlap region of the overlapping element $\mathcal{D}_I$:

If $I \neq J$, the nodal values $\hat{\varphi}_{Ji}^I$ are only nonzero with the weight functions given in Table 1 at the virtual node located at node J and the two virtual nodes adjacent to node J.

If $I = J$, the nodal values $\hat{\varphi}_{Ji}^I$ are only nonzero with the weight functions given in Table 1 at the virtual node located at node J and at the three mid-sides virtual nodes of the overlap region.

Fig. 3 gives the generic nodal values used in the interpolation functions $\hat{\varphi}_I^I(\mathbf{x})$, $\hat{\varphi}_J^I(\mathbf{x})$ and $\hat{\varphi}_K^I(\mathbf{x})$ for the overlap region $\mathcal{E}^m$ corresponding to the overlapping element $\mathcal{D}_I$. Table 1 gives the actual nodal values used based on the above criteria. We use, in this paper, the interpolation functions defined in Table 1, but other functions that satisfy Criteria I to III could also be established.

In Table 1, W_I is the weight function for node I and is chosen to be

$$W_I = \begin{cases} 1 - 6s^2 + 8s^3 - 3s^4 & 0 \leqslant s \leqslant 1 \\ 0 & s > 1 \end{cases} \tag{7}$$

with s given by

$$s = \frac{d_I}{r_I} \tag{8}$$

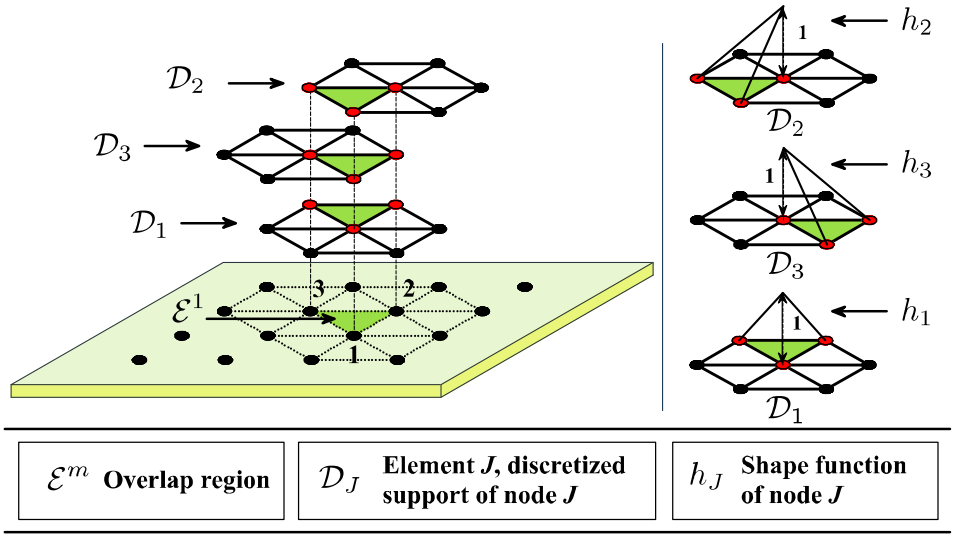

Fig. 4. Schematic of the interpolation process; in the overlap region $\mathcal{E}^1$, the local field of each overlapping element is constructed from the physical nodes listed in I_1 (see red nodes).

where d_I denotes the distance between node I and point $\mathbf{x} = (x, y)$, and r_I is the radius of $\mathcal{S}_I$. This radius is selected to contain all six triangular regions around node I, thus also defining the nodes in $\mathcal{N}_I$.

2.3. Global interpolation

Let $\{\mathcal{T}^h\} := \{\mathcal{E}^m\}_{m=1}^{e}$ be the e triangular overlap regions that together discretize the global analysis domain Ω

$$\bigcup_{m=1}^{e} \mathcal{E}^m = \Omega \tag{9}$$

Let I_m be the set of indices defined by

$$I_m := \{I : \mathcal{D}_I \cap \mathcal{E}^m \neq \varnothing\} \tag{10}$$

The global field is constructed from the local fields as

$$\mathbf{u}(\mathbf{x}) = \sum_{m=1}^{e}\sum_{I\in I_m} h_I \psi_I(\mathbf{x}) = \sum_{m=1}^{e}\sum_{I\in I_m} h_I \left(\sum_{J\in\mathcal{N}_I}\sum_{n\in\mathfrak{I}} \hat{\varphi}_J^I(\mathbf{x})(p_n \mathbf{a}_{Jn}) \right) \tag{11}$$

where $\psi_I(\mathbf{x})$ is the local field corresponding to node I (see Eq. (6)) and h_I is the Ith nodal shape function of the traditional triangular 3-node finite element (a partition of unity function). Since the local field in the overlap region $\mathcal{E}^m$ of each overlapping element is only constructed from the nodes listed in I_m, the global field of Eq. (11) can be written as

$$\mathbf{u}(\mathbf{x}) = \sum_{m=1}^{e}\sum_{I\in I_m} h_I \psi_I(\mathbf{x}) = \sum_{m=1}^{e}\sum_{I\in I_m} h_I \left(\sum_{J\in I_m}\sum_{n\in\mathfrak{I}} \hat{\varphi}_J^I(\mathbf{x})(p_n \mathbf{a}_{Jn}) \right) \tag{12}$$

Considering Fig. 4, we note that $\mathcal{D}_1$, $\mathcal{D}_2$, $\mathcal{D}_3$ are overlapping elements with $\mathcal{E}^1$ then the overlap region. The local field of the elements for the overlap region $\mathcal{E}^1$ is constructed from the nodes in I_1 and the displacement field thus constructed is continuous and is interpolated with polynomials (see Eqs. (6), (11) and (12)).

It is valuable to note that when the radius of the support function (in Eqs. (7) and (8)) becomes infinite, the triangular overlap region becomes the "3-node triangular finite element with interpolation covers"; for the formulation and theoretical foundation of these elements see Refs. [21,22] and the references therein. The details to reach this conclusion are presented in Appendix A.

We should also note that the element passes the basic numerical tests: it contains no spurious zero energy mode, satisfies the isotropy condition and passes the patch test [14]. The governing equations of the discretization are derived as in traditional finite element analysis, see e.g. Ref. [14].

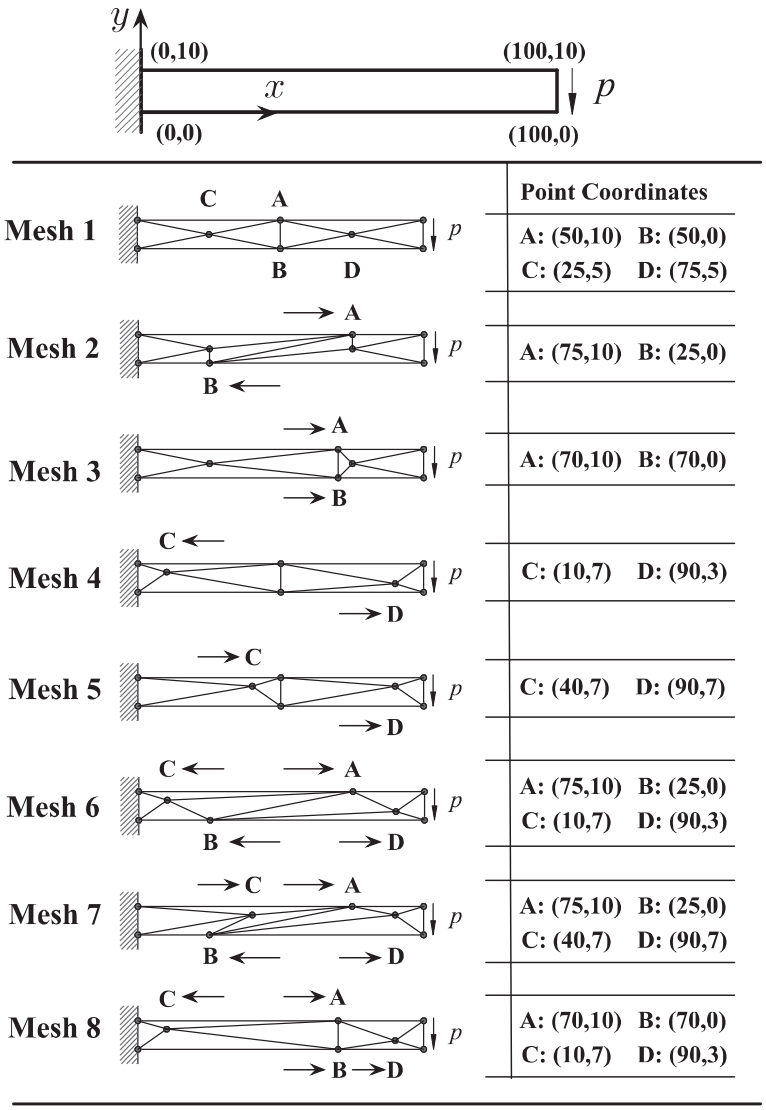

Fig. 5. Eight meshes used in the analysis of a cantilever beam problem; plane strain conditions, $p = 100, E = 200 \times 10^7, \upsilon = 0.3$.

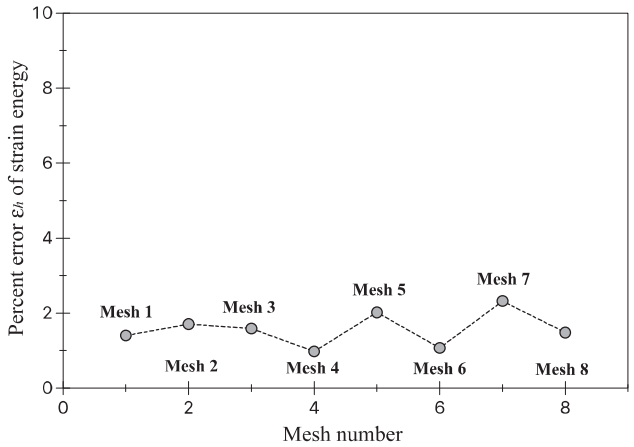

Fig. 6. Percent error ε_h of the strain energy obtained using the overlapping element; the reference solution is obtained using a mesh of 100×1000 9-node finite elements.

2.4. Numerical evaluation of element matrices

For the overlapping finite element we use the same order of numerical integration (9-point integration) as for the previously presented scheme [12]. However, whereas rational functions were integrated with a significant (albeit acceptable) integration error, for the scheme given here the numerical integration could give us the exact stiffness matrix (as analytically integrated). For the overlapping element, to obtain the exact stiffness matrix, theoretically, 12-point integration (which could accurately reproduce a polynomial of degree 6) is needed if the linear polynomial basis is used and 16-point integration (which could accurately reproduce a polynomial of degree 8) is needed if the quadratic polynomial basis is used. The computational efficiency of the overlapping element is studied in Section 3.1.

In two-dimensional solutions, we could use the higher integration orders without much effect on the total solution time, but in three-dimensional analyses, it is important to use an effective number of integration points (see Section 5).

2.5. Distortion insensitivity of the new element

An important advantage of the overlapping finite element in Ref. [12] is that the element is relatively distortion insensitive, that is, the solution accuracy is almost independent of the geometric shape of the element. Hence overlapping finite elements might be used effectively in the new paradigm of finite element analysis to couple regular meshes of traditional finite elements to the boundaries of complex geometries. To evaluate the distortion sensitivity of the above-presented overlapping finite element, we consider two numerical examples.

2.5.1. A cantilever beam analysis using distorted meshes

The cantilever beam already considered in Ref. [12] is used to study the performance of the overlapping element using distorted meshes. Fig. 5 shows the 8 meshes we use, each containing only 8 nodes, hence each mesh is quite coarse and very accurate results cannot be expected. We use the quadratic polynomial basis, 9-point numerical integration, and the Dirichlet boundary condition is imposed as discussed in our previous paper [12].

To show the performance of the overlapping element, the percent error ε_h of the strain energy is presented in Fig. 6. The error is for all meshes within about 1 to 3 percent illustrating that the new element is quite insensitive to mesh distortions, although these are quite high. The same conclusion was also reached in Ref. [12] for the element presented therein.

2.5.2. A shaft problem using distorted meshes

We use the shaft problem shown in Fig. 7 to study the energy convergence as the elements become distorted. In the study we compare the results with those obtained using the traditional 4-node finite elements and finite elements with interpolation covers [21]. Fig. 8 shows the meshes used. To identify the distortion sensitivity, we increase $\Delta\theta$ but keep one layer of undistorted finite elements at the Dirichlet boundary (similar to when using the new paradigm of finite element analysis). These elements are formulated as coupling elements, see Refs. [11,12], and the interpolation functions are

$$\mathbf{u}(\mathbf{x}) = \sum_{I\in\chi} h_I \left(h_I \mathbf{u}_I + \sum_{\substack{K\in\kappa \\ K\neq I}} h_K \mathbf{a}_{K1} \right) + \sum_{I=1}^{noe} h_I \hat{\psi}_I(\mathbf{x}) \tag{13}$$

where χ is the index set of the pure finite element nodes of the coupling region considered, h_I is Ith nodal shape function of the traditional triangular 3-node finite element, κ is the index set of all nodes of the element, $\mathbf{a}_{K1} = [a^u_{K1}\ a^v_{K1}]$ is the unknown solution vector of node K equal to $\mathbf{u}_K$, and *noe* is the number of overlapping elements which have an intersection with the element in the coupling

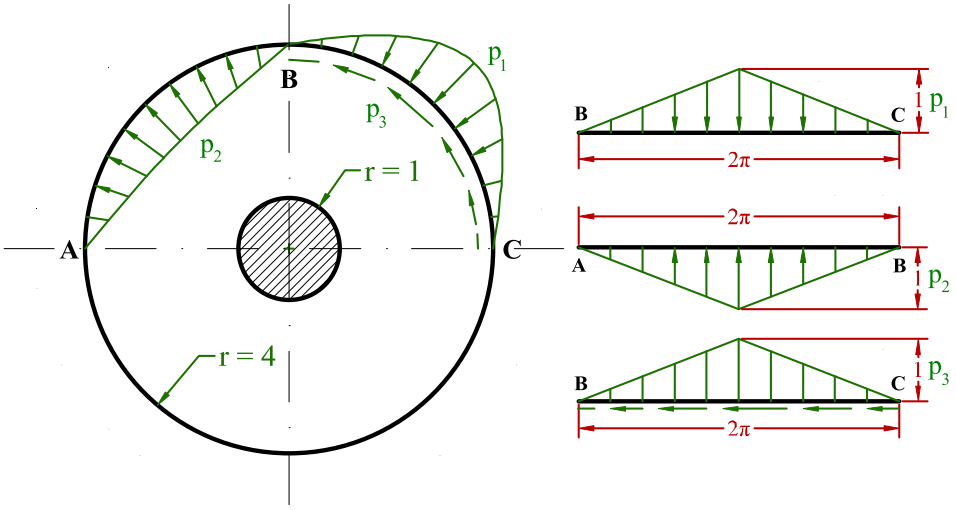

Fig. 7. A shaft fixed inside under plane strain conditions ($E = 100, \upsilon = 0.3$) with loads applied on the boundary, $p_1 = p_2 = p_3 = 1.0$.

region, see Refs. [11,12] for a detailed discussion. In Eq. (13), the local field $\hat{\boldsymbol{\psi}}_I(\mathbf{x})$ is given as

$$\hat{\boldsymbol{\psi}}_I(\mathbf{x}) = \sum_{\substack{J\in\mathcal{N}_I \\ J\neq\chi}} \hat{\varphi}_J^I(\mathbf{x}) \sum_{n\in\Im} (p_n \mathbf{a}_{Jn}) + \sum_{J\in\chi} \hat{\varphi}_J^I(\mathbf{x}) \left(h_J \mathbf{u}_J + \sum_{\substack{K\in\kappa \\ K\neq J}} h_K \mathbf{a}_{K1} \right) \tag{14}$$

The finite elements with interpolation covers use the same mesh (as shown in Fig. 8(a)). To impose the Dirichlet boundary conditions, no cover degrees of freedom are assigned for nodes on the boundary.

To study the energy convergence, the strain energy E_h is calculated as the mesh is refined in the radial direction. The convergence of the strain energy is obtained using meshes with various $\Delta\theta$ values.

Fig. 9 shows the mesh with 36×6 nodes ($\Delta\theta = \pi/12$) used in the distortion study. Table 2 lists the strain energy error for the scheme using the overlapping element (referred to as the "new scheme" here and below), the finite element with quadratic covers and the 4-node finite element. Fig. 10 shows the energy error as a function of h, which is the element length in the radial direction. As we see in Fig. 10, the solution accuracy using the 4-node finite element and the finite element with interpolation covers decreases with increasing element distortions. Indeed, the rate of convergence using the 4-node finite element is practically zero for $\Delta\theta = \pi/12$. On the other hand, the solution accuracy of the new scheme is hardly affected by the element distortions. Here the rate of convergence of the solutions using the overlapping finite element is only about 2 (see Fig. 10) because we use one layer of linear triangular elements at the Dirichlet boundary.

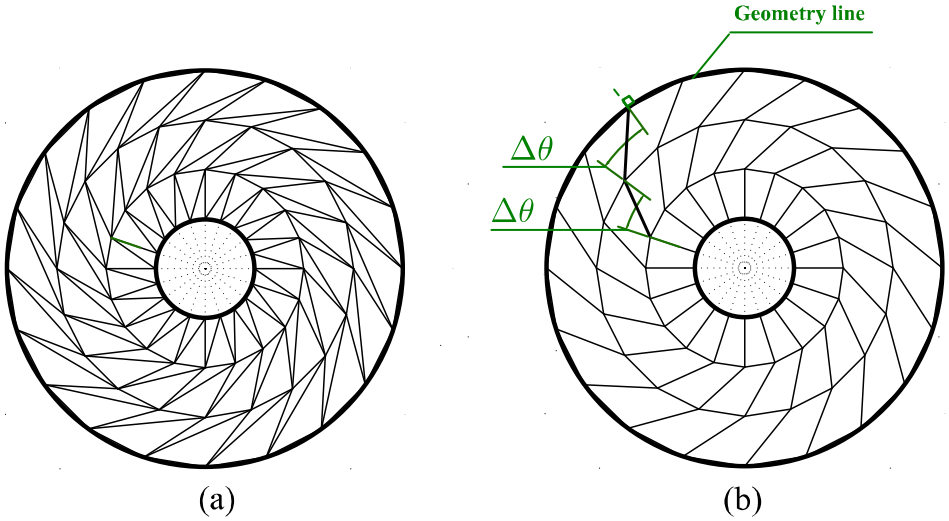

Fig. 8. Meshes using 20×4 nodes for the element distortion study, the nodes are equally distributed along both the tangential and radial directions, h is the element length in the radial direction; (a) mesh of the overlapping element and the finite element with covers; (b) mesh of the traditional 4-node finite element.

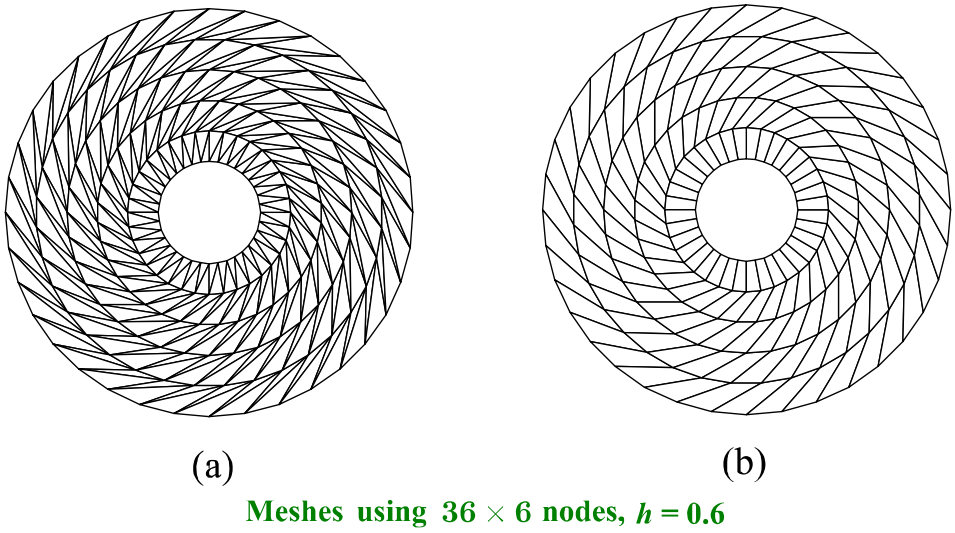

Fig. 9. Meshes using 36×6 nodes ($\Delta\theta = \pi/12$); (a) mesh of the overlapping element and the finite element with covers; (b) mesh of the traditional 4-node finite element.

3. Computational efficiency of the new paradigm

In this section we investigate the computational efficiency of the new paradigm of solutions. We study the required numerical integration, total number of degrees of freedom, half-bandwidth of the stiffness matrix and the computational effort expended in solving the governing finite element equations.

3.1. Computational efficiency of the numerical integration

To study the computational effort in the numerical integration, we consider the meshes shown in Fig. 11 and evaluate the required runtime to obtain the element matrices, when using the overlapping element and the traditional 4-node finite element (we use the QUADS code from Ref. [14]). Table 3 shows the total number of integration points, the total number of degrees of freedom and the CPU time used for the numerical integration as the h-type uniform refinement is performed. The CPU time is the total runtime for computing the element matrices of the stiffness matrix from all integration domains. We obtained the results using a laptop with a single core 3 GHz Intel i7 CPU.

Fig. 12 presents the CPU time of the numerical integration as a function of the total number of degrees of freedom. Clearly, in each case, the numerical integration effort increases linearly with the

Table 2
Strain energy error (rounded) of the new scheme with overlapping finite elements, finite elements with interpolation covers and using 4-node finite elements for various $\Delta\theta$; h is the "element length" in the radial direction. The reference strain energy E_{ref} is obtained using a mesh of 36×30 nodes ($\Delta\theta = 0$) of finite elements with quadratic interpolation covers.

Nodes in mesh	h	$\log(\lvert E_{ref} - E_h \rvert / E_{ref})$			
		$\Delta\theta = 0$	$\Delta\theta = \pi/36$	$\Delta\theta = \pi/18$	$\Delta\theta = \pi/12$
New scheme with overlapping finite elements (quadratic polynomial basis)					
36×4	1.00	−2.32	−2.30	−2.27	−2.26
36×5	0.75	−2.57	−2.57	−2.56	−2.55
36×6	0.60	−2.76	−2.80	−2.80	−2.79
36×7	0.50	−2.95	−2.98	−2.99	−2.97
Finite elements with quadratic covers					
36×4	1.00	−2.06	−2.03	−1.97	−1.95
36×5	0.75	−2.28	−2.23	−2.21	−2.18
36×6	0.60	−2.46	−2.42	−2.39	−2.37
36×7	0.50	−2.61	−2.58	−2.55	−2.51
4-node finite elements					
36×4	1.00	−1.43	−1.40	−1.34	−1.26
36×5	0.75	−1.60	−1.55	−1.44	−1.31
36×6	0.60	−1.72	−1.65	−1.49	−1.30
36×7	0.50	−1.81	−1.71	−1.50	−1.27

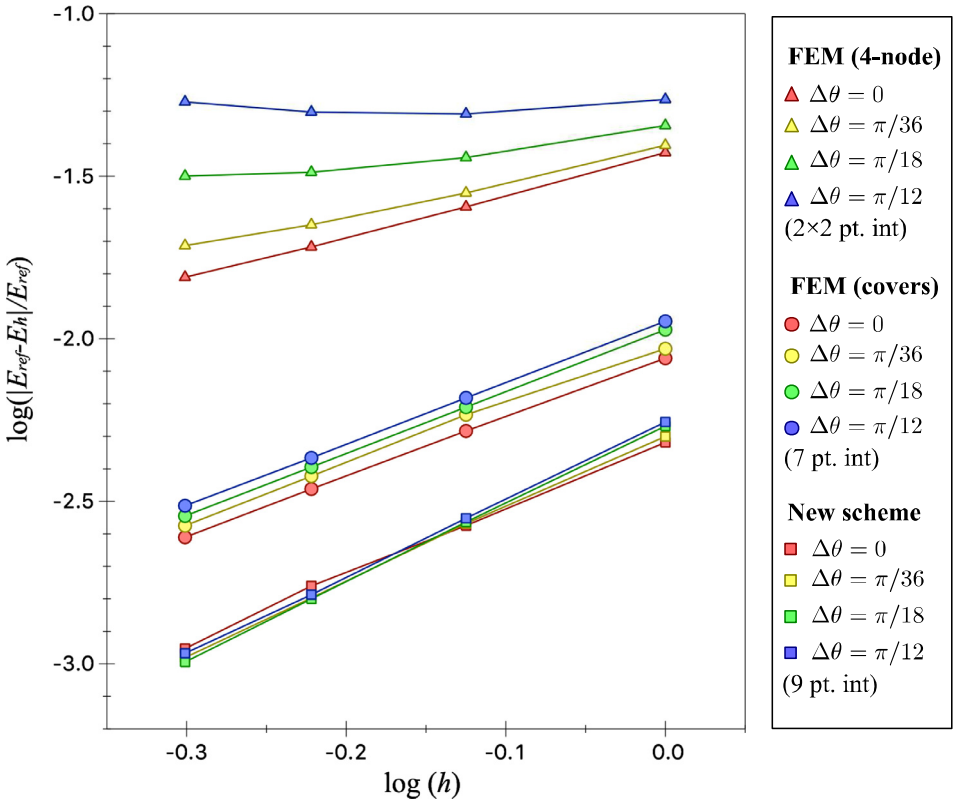

Fig. 10. Convergence of strain energy for various methods; using the traditional 4-node finite element, the finite element with interpolation covers, and the new scheme; quadratic polynomial covers are used with 7-point integration in each element; overlapping elements are used with the quadratic polynomial basis and 9-point integration in each overlap region.

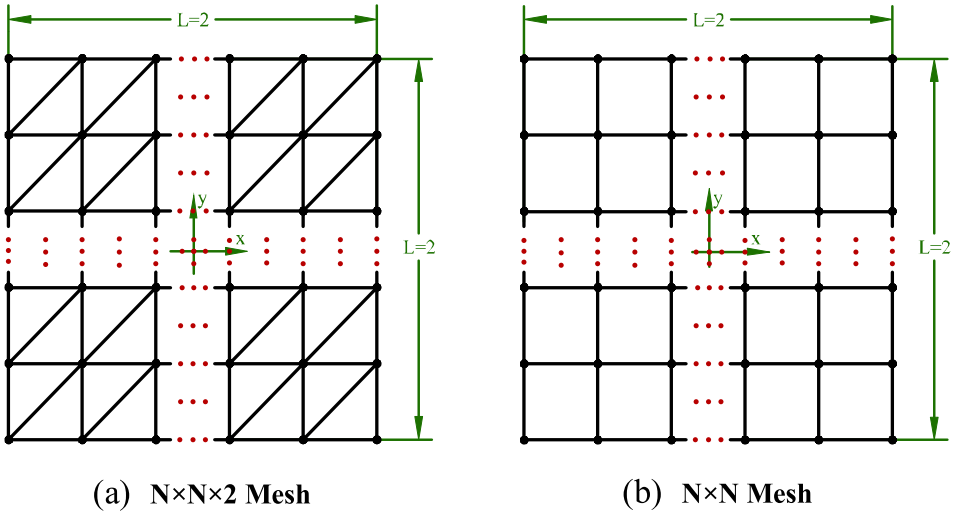

Fig. 11. Meshes for the numerical integration study; (a) $N \times N \times 2$ mesh of overlapping elements; (b) $N \times N$ mesh of traditional 4-node finite elements; $E = 100, \upsilon = 0.3$; meshes are generated with $N + 1$ nodes equally distributed along the x and y directions.

Table 3
The total number of integration points, total number of degrees of freedom and CPU times used for the numerical integrations, only two entries for each case need be given.

Mesh	Total number of integration points	Total number of degrees of freedom	CPU time (s)
4-node finite elements			
50×50	2500×4	5.20×10^3	1.52×10^{-2}
800×800	$640{,}000 \times 4$	1.28×10^6	3.54×10^0
Overlapping finite elements (bilinear polynomial basis)			
$50 \times 50 \times 2$	5000×9	2.08×10^4	3.25×10^{-2}
$500 \times 500 \times 2$	$500{,}000 \times 9$	2.01×10^6	3.32×10^0
Overlapping finite elements (quadratic polynomial basis)			
$50 \times 50 \times 2$	5000×9	3.12×10^4	5.89×10^{-2}
$500 \times 500 \times 2$	$500{,}000 \times 9$	3.01×10^6	6.03×10^0

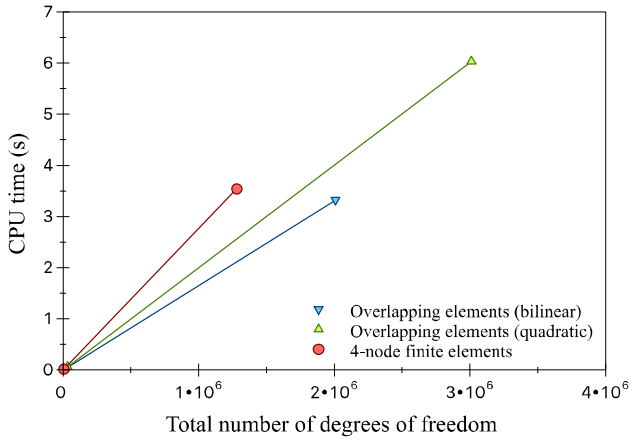

Fig. 12. CPU time for the numerical integration as a function of the total number of degrees of freedom; for the overlapping finite elements, 9-point integration is used; for the 4-node finite elements, 2×2 Gauss integration is used.

number of elements used. We observe that measured on the number of degrees of freedom used, the numerical effort in the integration is less for the overlapping finite elements than for the

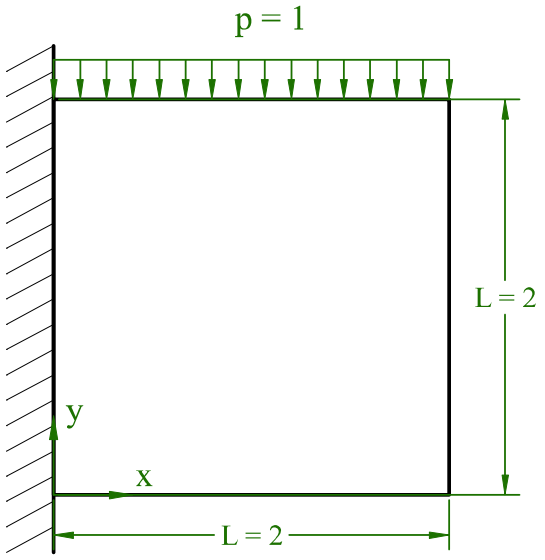

Fig. 13. A cantilever plate in plane strain conditions subjected to a uniformly distributed load p per unit length; $E = 100$, $\upsilon = 0.3$.

traditional finite elements. While, of course, additional considerations are important when considering the overall efficiency of using the elements, we see that the effort used in the numerical integration is quite reasonable. For the illustrative examples in Section 4, the computational time used for the numerical integration is always small.

3.2. Computational efficiency in the analysis of a cantilever plate problem

We solve the cantilever plate problem (see Fig. 13) already considered earlier [11] to study the computational efficiency of the new paradigm of solutions. Fig. 14 shows the meshes employed. In the new paradigm of solutions, the rectangular coupling regions are used because a bilinear polynomial field is then accurately reproduced (see the coupling schemes proposed in Refs. [11,12]).

In our studies we used the column reduction solver COLSOL [14] but of course in practice a sparse solver would be employed. To

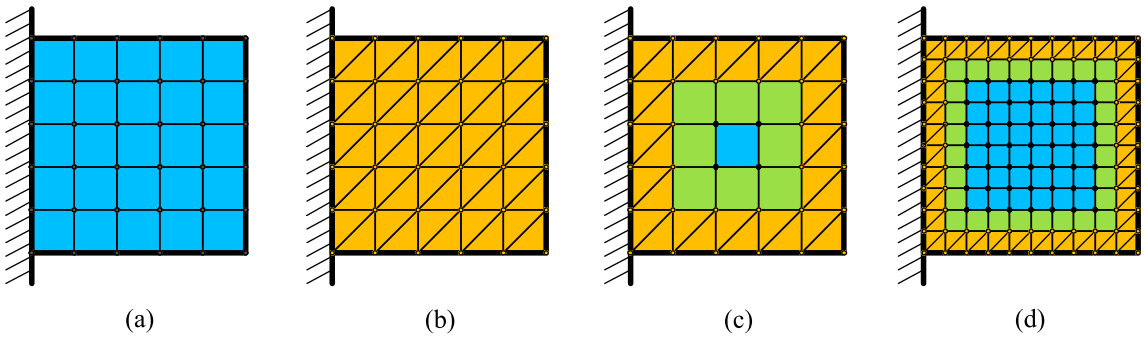

Fig. 14. Meshes of the cantilever plate equally discretized in the vertical and horizontal directions; (a) mesh of traditional 4-node finite elements (blue regions represent the 4-node finite elements); (b) mesh of overlapping finite elements (orange regions represent the overlap regions) and of finite elements using covers; (c) mesh of the new paradigm (green regions represent the coupling regions); (d) a mesh of the new paradigm as the uniform mesh refinement is performed (always two layers of overlapping elements are used near the boundary).

Table 4
Analysis of cantilever plate using 4-node finite elements, finite elements with interpolation covers, overlapping finite elements and the new paradigm scheme; strain energy error and total number of degrees of freedom.

h	$log(\lvert E_{ref} - E_h \rvert / E_{ref})$	Total number of degrees of freedom
4-node finite elements		
0.4	−1.23	60
0.2	−1.65	220
0.1	−2.08	840
0.04	−2.65	5100
0.02	−3.09	20,200
Finite elements with bilinear covers		
0.4	−1.65	240
0.2	−2.07	880
0.1	−2.50	3360
0.04	−3.07	20,400
Finite elements with quadratic covers		
0.4	−1.88	360
0.2	−2.31	1320
0.1	−2.74	5040
0.04	−3.32	30,600
Overlapping finite elements (bilinear polynomial basis)		
0.4	−2.42	264
0.2	−2.82	924
0.1	−3.25	3444
0.04	−3.84	20,604
Overlapping finite elements (quadratic polynomial basis)		
0.4	−3.04	396
0.2	−3.44	1386
0.1	−3.91	5166
0.04	−4.88	30,906
New scheme (bilinear polynomial basis)		
0.4	−2.36	240
0.2	−2.54	630
0.1	−2.84	1710
0.04	−3.35	7350
0.02	−3.78	24,750
New scheme (quadratic polynomial basis)		
0.4	−2.65	356
0.2	−2.67	896
0.1	−2.94	2276
0.04	−3.44	8816
0.02	−3.87	27,716

measure the computational effort for the solution of the finite element equations we can thus use

$$SolE = \frac{1}{2}\sum_{i=1}^{n} m_i^2 \tag{15}$$

where n denotes the total number of degrees of freedom and m_i denotes the column height of column i (including the zero elements in the column [14]). This measure can be useful to predict a required solution effort prior to an actual analysis run as we show also below.

Table 4 lists the strain energy errors and total number of degrees of freedom of the solution schemes as the h-type uniform refinement is performed. To establish the reference strain energy for comparison, we used a mesh of 300×300 traditional 9-node finite elements. For the overlapping finite elements, we always used 9-point integration and for finite elements with interpolation covers we always used 7-point integration.

Table 5 shows the actual and predicted CPU times used for the coarsest mesh solutions referred to in Table 4 that gave at least an energy error of 10^{-3}. We obtained all solutions on a laptop with a single core 3 GHz Intel i7 CPU. To predict the solution times (*SolE*), we used the actual CPU time for the solution of the traditional 4-node finite element mesh as reference and scaled that solution time using Eq. (15).

We see that in this analysis using the proposed new paradigm scheme with the bilinear basis for the overlapping finite elements requires much less computational time than using the 4-node finite element mesh. This is because the force (natural) boundary conditions can be more accurately captured with the overlapping finite elements. Indeed, in this case the use of the overlapping finite elements for the complete domain of analysis is computationally very effective, whereas the use of finite elements with covers is not leading to an efficient solution.

Fig. 15 shows the convergence in strain energy as the meshes are refined, as also given in Table 4. The figure shows that the orders of convergence (the slopes of the curves) are almost the same for the schemes (with the overlapping finite element using the quadratic basis reaching for small h a better order), but the rate (which includes the constant, i.e. shift down of the curve [14]) is the worst when using the traditional 4-node finite element. The figure also shows that different meshes need to be used *to achieve a given level of accuracy*, as employed in Table 5, and shows that in this example solution the use of overlapping elements for the complete analysis domain can *then* be competitive.

Table 6 shows that the use of the new scheme is effective, and indeed in this example also using only overlapping finite elements is quite effective. Here we give the actual and predicted solution times when refining the mesh as given in Table 4. We also list in this table the time used for the numerical integration in the finest mesh used. This time can be linearly scaled to any mesh employed.

Table 5
Actual and predicted CPU times (both rounded) for the solution of the finite element equations analyzing the cantilever plate for the coarsest meshes with a strain energy error of at least 10^{-3} .

Scheme		$\log(\lvert E_{ref} - E_h\rvert / E_{ref})$	Actual CPU time (s)	Predicted CPU time *SolE* (s)
4-node finite elements		−3.09	1.3	–
Finite elements with covers	Bilinear basis	−3.07	5.1	5.4
	Quadratic basis	−3.32	18	19
Overlapping finite elements	Bilinear basis	−3.25	0.16	0.16
	Quadratic basis	−3.04	0.007	0.004
New scheme	Bilinear basis	−3.35	0.4	0.4
	Quadratic basis	−3.44	1.0	1.0

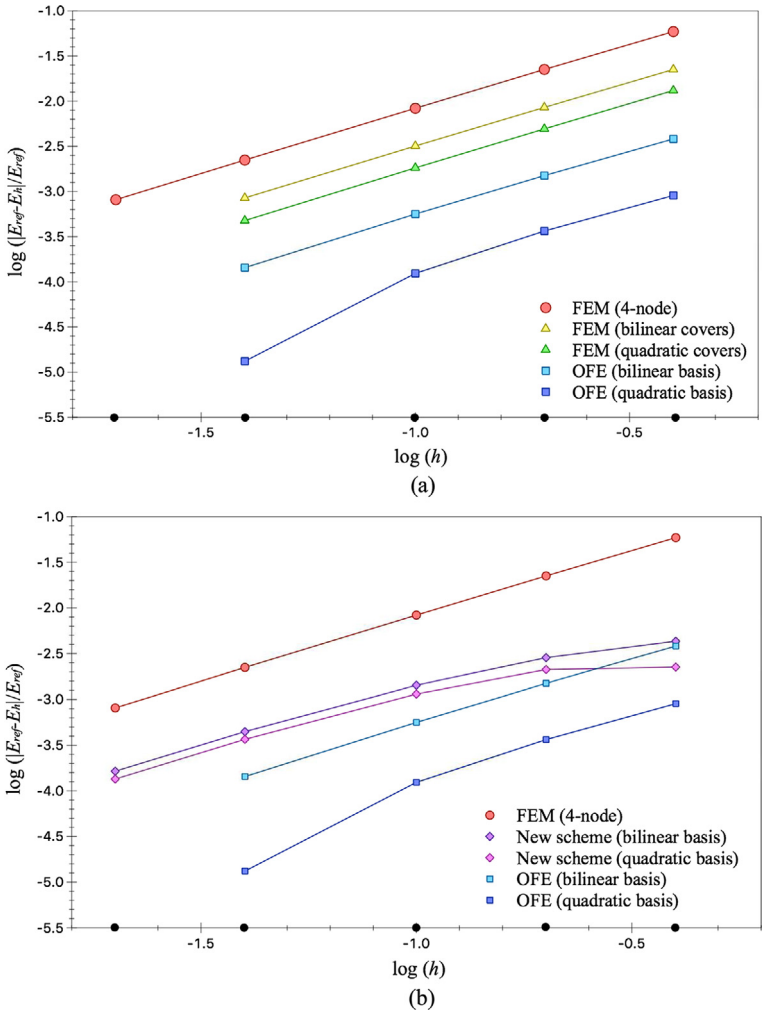

Fig. 15. The energy convergence curves with various methods; OFE denotes the overlapping finite element.

For a fine mesh, the time is always small compared to the time required for the solution of the equations, and indeed for the given entries in Table 6 the time used for the numerical integration is about two of magnitude smaller.

4. The new paradigm used to solve a cantilever plate with holes problem

In this section, we illustrate the complete procedure of the new paradigm of solutions (with the overlapping element) by solving a cantilever plate with holes (see Fig. 16). We illustrate that using the new meshing scheme, the geometrical defects in the CAD geometry of the plate can be automatically removed and obtain the solutions for two load cases (see Fig. 17.).

The new scheme consists of four steps, see Refs. [10,11]. As shown in Fig. 18, in the first step the algorithm immerses the cantilever plate in a Cartesian grid. In the second step the boundaries are discretized with straight line segments Δs, during which the three geometry deficiencies are automatically removed (see Fig. 18(b)). Thereafter, in the third step the algorithm converts

Table 6
Analysis of cantilever plate; strain energy error, numerical integration time, actual and predicted times to solve the governing finite element equations; all times are rounded.

h	$log(\|E_{ref} - E_h\|/E_{ref})$	Numerical integration time (s)	Actual CPU time (s)	Predicted CPU time *SolE* (s)
4-node finite elements				
0.4	−1.23		Order of 10^{-5}	Order of 10^{-5}
0.2	−1.65		Order of 10^{-4}	Order of 10^{-4}
0.1	−2.08		2.9×10^{-3}	2.5×10^{-3}
0.04	−2.65		9.0×10^{-2}	8.6×10^{-2}
0.02	−3.09	5.5×10^{-2}	1.3×10^{0}	–
Finite elements with bilinear covers				
0.4	−1.65		1.4×10^{-3}	1.0×10^{-3}
0.2	−2.07		1.4×10^{-2}	1.1×10^{-2}
0.1	−2.50		1.5×10^{-1}	1.5×10^{-1}
0.04	−3.07	3.5×10^{-2}	5.1×10^{0}	5.4×10^{0}
Finite elements with quadratic covers				
0.4	−1.88		3.9×10^{-3}	3.5×10^{-3}
0.2	−2.31		4.2×10^{-2}	4.2×10^{-2}
0.1	−2.74		5.3×10^{-1}	5.5×10^{-1}
0.04	−3.32	6.8×10^{-2}	$1.8 \times 10^{+1}$	$1.9 \times 10^{+1}$
Overlapping finite elements (bilinear polynomial basis)				
0.4	−2.42		2.0×10^{-3}	1.0×10^{-3}
0.2	−2.82		1.3×10^{-2}	1.2×10^{-2}
0.1	−3.25		1.6×10^{-1}	1.6×10^{-1}
0.04	−3.84	3.4×10^{-2}	5.4×10^{0}	5.5×10^{0}
Overlapping finite elements (quadratic polynomial basis)				
0.4	−3.04		6.8×10^{-3}	4.0×10^{-3}
0.2	−3.44		4.5×10^{-2}	4.4×10^{-2}
0.1	−3.91		5.4×10^{-1}	5.7×10^{-1}
0.04	−4.88	7.7×10^{-2}	$1.9 \times 10^{+1}$	$1.9 \times 10^{+1}$
New scheme (bilinear polynomial basis)				
0.4	−2.36		1.1×10^{-3}	1.0×10^{-3}
0.2	−2.54		6.1×10^{-3}	4.5×10^{-3}
0.1	−2.84		2.8×10^{-2}	2.8×10^{-2}
0.04	−3.35		3.9×10^{-1}	4.0×10^{-1}
0.02	−3.78	6.8×10^{-2}	3.5×10^{0}	3.7×10^{0}
New scheme (quadratic polynomial basis)				
0.4	−2.65		4.7×10^{-3}	2.8×10^{-3}
0.2	−2.67		1.5×10^{-2}	1.4×10^{-2}
0.1	−2.94		8.4×10^{-2}	8.0×10^{-2}
0.04	−3.44		1.0×10^{0}	1.0×10^{0}
0.02	−3.87	7.1×10^{-2}	8.2×10^{0}	8.3×10^{0}

the internal cells into traditional finite elements. Finally, in the fourth step the algorithm covers the empty space with overlapping finite elements (see Fig. 18(d)).

In order to compare the traditional finite element analysis with the new paradigm of solutions, we also solve the problem using only the 4-node finite element. Fig. 19 shows the mesh of the traditional 4-node finite element and the new scheme using the traditional 4-node element and the overlapping element, with coupling regions. Table 7 gives the total number of equations, calculated strain energies and computational efforts used in both solutions. Figs. 20 and 21 show the resulting stress plots; with τ_{yy}^{h} and τ_{yy}^{ref} denoting the predicted and reference normal stresses (obtained with the very fine mesh of 9-node finite elements). We see that the new scheme gives a slightly higher strain energy for the load case of the tangential traction (indicating a more accurate solution [14]), and smoother stress fields with smaller absolute stress errors for both load cases. Table 7 shows that the computational effort for solving the finite element equations using the new scheme is not much higher than when performing the traditional analysis, although COLSOL was used with no optimization on the ordering of the equations for the new scheme (while the ordering of the equations was optimized for the traditional analysis). The table also shows that the CPU time used for the numerical integra-

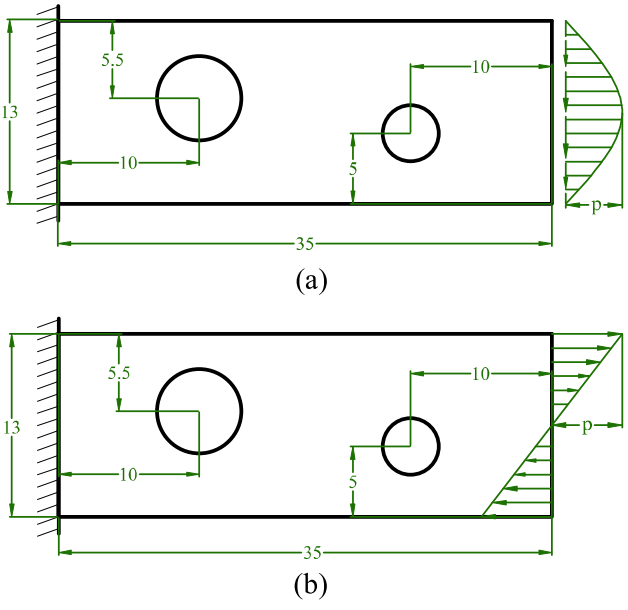

Fig. 16. Cantilever plate in plane stress conditions ($E = 200 \times 10^9$, $\upsilon = 0.3$, thickness = 1.0), radii of holes = 2 and 3; (a) quadratic tangential traction; (b) linear normal pressure; p = 1000.

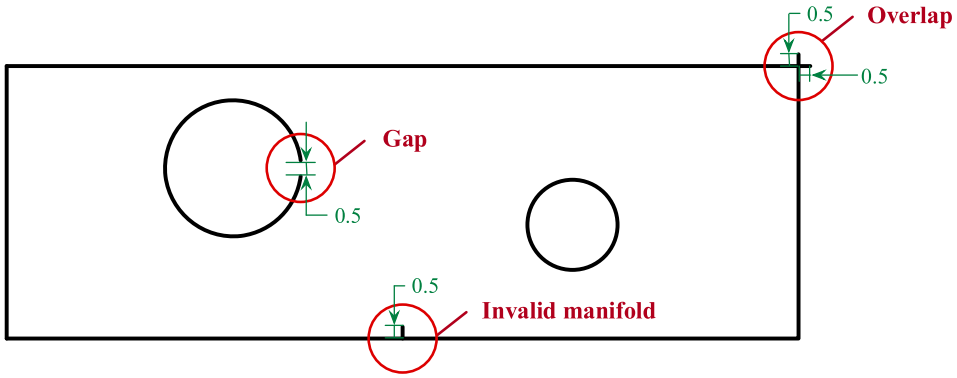

Fig. 17. A CAD representation of the cantilever plate; three geometrical imperfections.

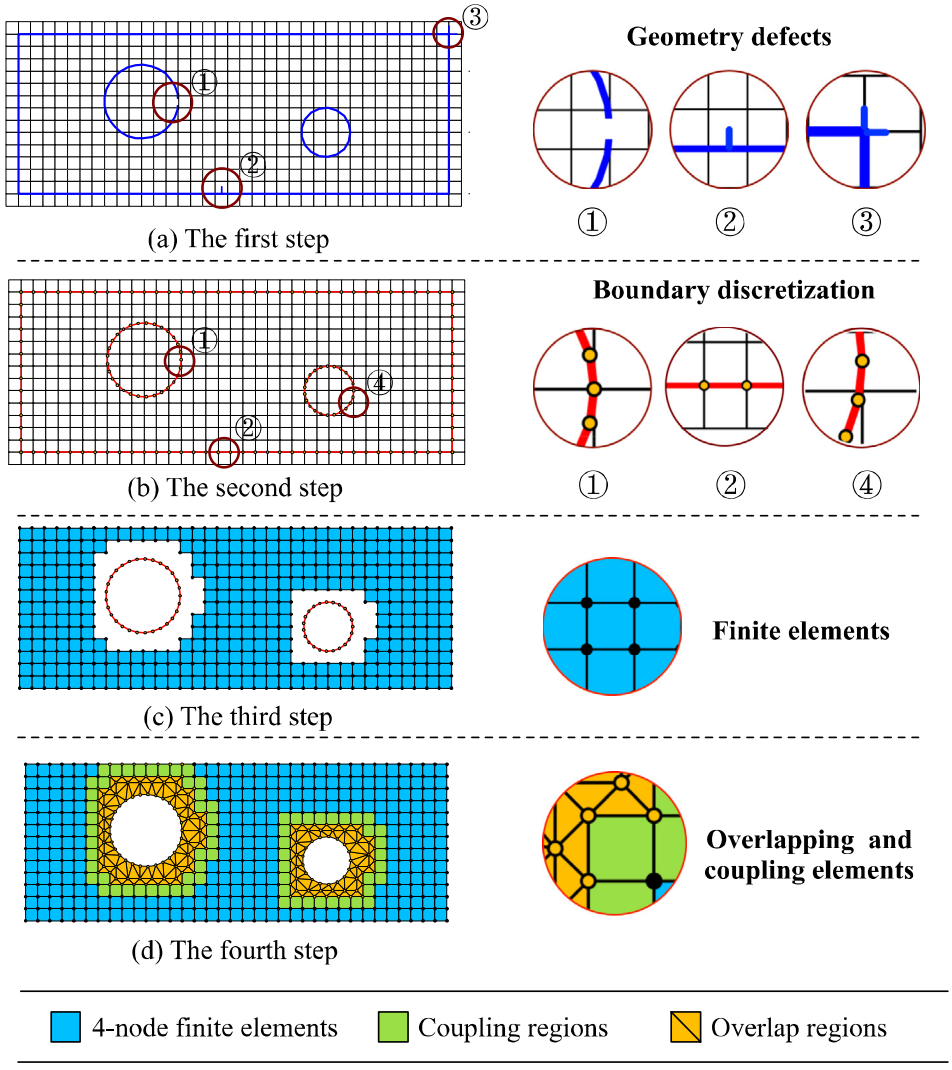

Fig. 18. The steps of the new meshing scheme; (a) the generated Cartesian grid; ① gap; ② invalid manifold; ③ overlap; (b) the straight line Δs - segmentation of the boundary, 3 different defects are removed; ① Δs_1 - segmentation; ② Δs_2 - segmentation; ④ Δs_3 - segmentation; (c) the internal cells retained and converted to 4-node traditional finite elements; (d) overlapping finite elements used to fill in empty space.

tion is in this analysis, for the new scheme, about two orders of magnitude smaller than required for the solution of the equations. Hence in this analysis, the new paradigm of solution clearly resulted into an overall effective solution.

5. A few remarks on 3D solutions

In this Section, we briefly comment on the computational effort of using the overlapping finite elements in the solution of three-

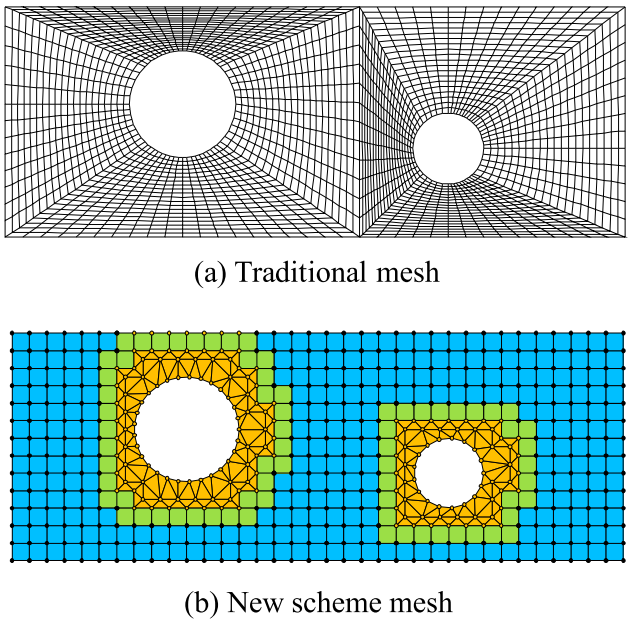

Fig. 19. The meshes of the traditional 4-node finite element and the new scheme with the 4-node finite element and the overlapping element; for the overlapping element, the bilinear polynomial basis is used with 9-point integration; for the traditional finite element 2×2 Gauss integration is used; in the coupling regions 3×3 Gauss integration is used.

dimensional (3D) problems. The computational effort in solving the equations is determined by Eq. (15). In the solution of 3D problems the total number of degrees of freedom and the column heights can become very large, and our objective is here to obtain only some insight into the use of the overlapping finite elements. We only solve a single problem, see Fig. 22, and consider the discretizations of the structure shown in Fig. 23. The structure is in essence the plate in Fig. 13 extruded into the third direction. Tables 8 and 9 give the solution times and the time for the numerical integrations for the different discretizations used. For the new elements, we use the scheme of Ref. [23] with 15 integration points in each overlap region. The reference strain energy was obtained using a very fine mesh of traditional 27-node elements.

We see that the solution times using the overlapping finite elements are quite reasonable when considering about the same accuracy reached as with the traditional 8-node element. Of course, detailed further studies are required to investigate the performance of the new overlapping elements and the new paradigm of solution considering the accuracy reached, like we have pursued above in the analyses of two-dimensional problems.

6. Concluding remarks

The objective in this paper was to present a new overlapping element that is significantly more effective than the previously proposed elements, including the disks/spheres in the method of finite spheres.

The important step is that we interpolate the Shepard function by polynomials over the triangular domain and then use in the global field interpolation only the solution unknowns corresponding to the three corner nodes of the triangular overlap region. We therefore do not integrate rational functions in the formulation

Table 7
Analysis of the cantilever plate example: comparison of the calculated strain energy, total number of degrees of freedom, time used for the numerical integration time and the time used for the solution of the equations.

Load case	Strain energy	Total number of degrees of freedom	Numerical integration time (s)	Actual CPU time (s)
Mesh, 4-node elements				
Tangential traction	1.80×10^{-2}	4986	1.4×10^{-2}	2.6×10^{-1}
Normal pressure	4.00×10^{-4}			
New meshing scheme				
Tangential traction	1.82×10^{-2}	2032	3.5×10^{-3}	3.0×10^{-1}
Normal pressure	4.00×10^{-4}			

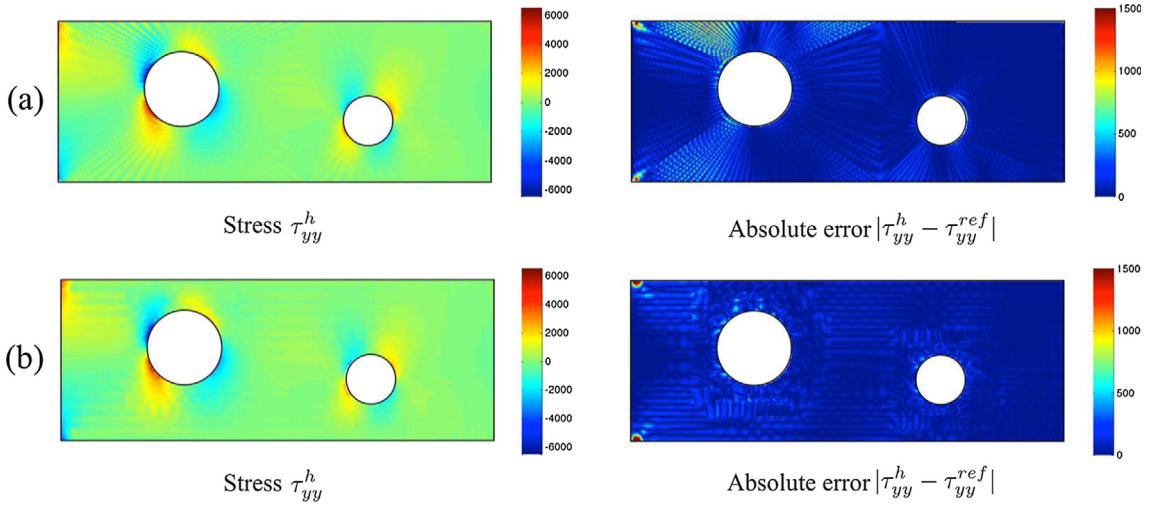

Fig. 20. Stress τ_{yy}^h and absolute error $|\tau_{yy}^h - \tau_{yy}^{ref}|$ in case of tangential traction; (a) 4-node finite element mesh; (b) new scheme mesh.

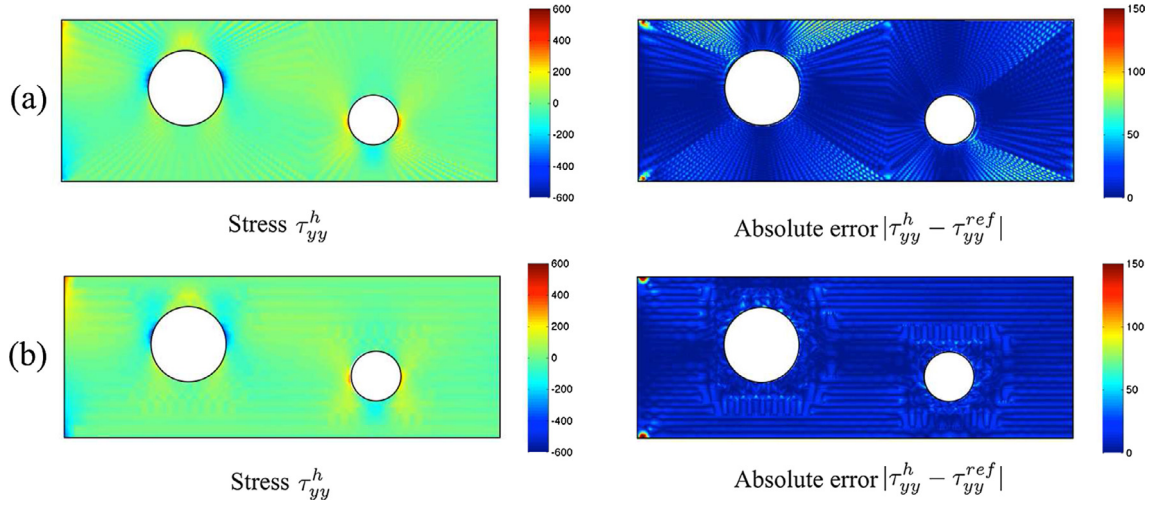

Fig. 21. Stress τ_{yy}^h and absolute error $|\tau_{yy}^h - \tau_{yy}^{ref}|$ with linear normal pressure; (a) 4-node finite element mesh; (b) new scheme mesh.

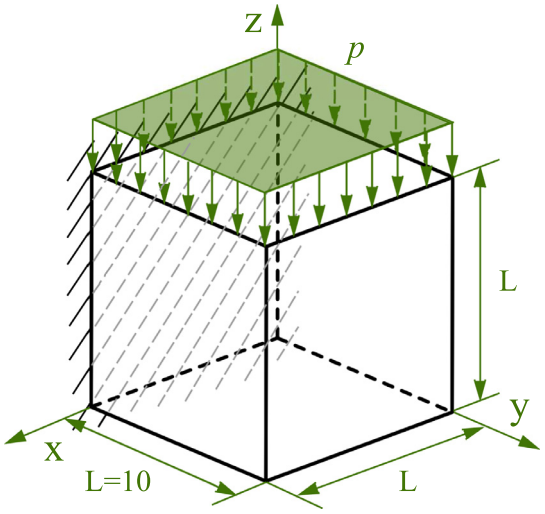

Fig. 22. A cubic structure subjected to a uniformly distributed load $p = 1.0$ on its top; $E = 100, \upsilon = 0.3$.

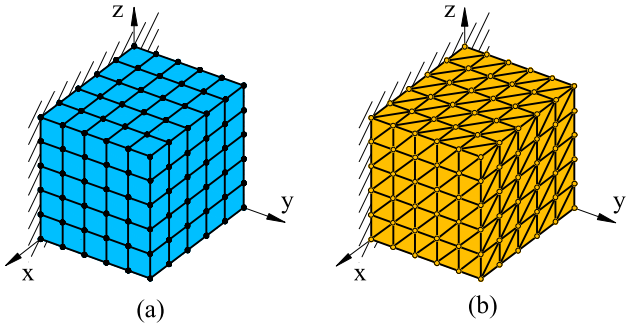

Fig. 23. Meshes of the structure equally discretized in the x, y, z directions; (a) mesh of the 8-node traditional finite element (b) mesh of the overlapping finite elements.

(avoiding the need of a high-order numerical integration) and the bandwidth of the resulting stiffness matrix is, in essence, as for traditional finite elements, but accounting for the fact that at each element node the number of unknowns is equal to the number of polynomials used in the basis of the element formulation. We also pointed out how the element relates to the finite elements with covers.

The interpolation of the Shepard function by polynomials to avoid the numerical integration of rational functions may also be effective in other procedures, like meshless methods.

We illustrated the effectiveness of the new overlapping element in various examples, in which we focused on the insensitivity of the element to geometric distortions, the rate of convergence reached, and the computational time used. We also illustrated the use of the element in an example solution using the new paradigm of analysis for meshing a solution domain.

However, the computational times reported for these studies are based on using a standard column reduction equation solver when in practice a sparse solver would be employed. Since the final columns in our studies are established during the assemblage of the finite element equations, we could employ an effective estimator for the solution times used and thus obtain insight into the new discretization scheme.

While we considered in depth only 2D problems, we also commented briefly on the use of the discretization scheme in 3D analyses.

We can conclude that the solution scheme presented in this paper is very promising, but more research on overlapping finite elements is needed — to study the proposed element further and develop and study new elements, for 2D and 3D solutions, incompressible media, shells, for linear and nonlinear, static and dynamic analyses, and so on. Using such elements in the new paradigm of analysis should lead to effective finite element procedures for use in computer-aided design and hence to the wide democratization of numerical simulations.

Table 8
Analysis of the 3D structure using 8-node brick elements, strain energy error, numerical integration time, actual and predicted times to solve the governing finite element equations; all times are rounded.

Mesh	$log(\lvert E_{ref} - E_h \rvert / E_{ref})$	Numerical integration time (s)	Actual CPUtime (s)	Predicted CPU time *SolE* (s)
8-node finite elements				
$10 \times 10 \times 10$	−1.65		6.4×10^{-1}	–
$20 \times 20 \times 20$	−2.09		$6.6 \times 10^{+1}$	$6.4 \times 10^{+1}$
$30 \times 30 \times 30$	−2.36	1.1×10^{0}	$1.0 \times 10^{+3}$	$1.0 \times 10^{+3}$

Table 9
Analysis of the 3D structure, strain energy error, numerical integration time, actual and predicted solution effort using overlapping finite elements; all times are rounded.

Mesh	$log(\lvert E_{ref} - E_h\rvert / E_{ref})$	Numerical integration time (s)	Actual CPU time (s)	Predicted CPU time *SolE* (s)
Overlapping finite elements (linear polynomial basis)				
$5 \times 5 \times 5$	−1.74		4.2×10^{-1}	4.1×10^{-1}
$8 \times 8 \times 8$	−2.04		8.7×10^{0}	8.4×10^{0}
$10 \times 10 \times 10$	−2.19		$4.0 \times 10^{+1}$	$3.7 \times 10^{+1}$
$15 \times 15 \times 15$	−2.46	5.3×10^{0}	$5.3 \times 10^{+2}$	$5.5 \times 10^{+2}$
Overlapping finite elements (quadratic polynomial basis)				
$5 \times 5 \times 5$	−2.17		7.8×10^{0}	7.0×10^{0}
$8 \times 8 \times 8$	−2.49		$1.3 \times 10^{+2}$	$1.4 \times 10^{+2}$
$10 \times 10 \times 10$	−2.65		$5.6 \times 10^{+2}$	$6.0 \times 10^{+2}$
$15 \times 15 \times 15$	−2.98	$3.2 \times 10^{+1}$	$8.4 \times 10^{+3}$	$8.9 \times 10^{+3}$

Appendix A. The finite element enriched by interpolation covers as a special case of the overlapping element

We show here how the proposed approximation scheme (see Eq. (12)) relates to the scheme of enriching finite elements by interpolation covers, see Ref. [21] and the references therein.

For a triangular overlap region as shown in Fig. A1, the global field of Eq. (12) can be written in the form

$$\mathbf{u} = \sum_{J=1}^{3} f_J \sum_{n \in \mathfrak{I}} p_n \mathbf{a}_{Jn} \tag{1.1}$$

where

$$f_J = \sum_{I=1}^{3} h_I \hat{\varphi}_J^I \tag{1.2}$$

Using the interpolation functions defined in Table 1 for $\hat{\varphi}_J^I$, $I,J = 1,2,3$, the $f_J, J = 1,2,3$, are

$$\begin{aligned}
f_1 &= \hat{h}_1 + \hat{h}_4(h_1+h_2)\frac{W_1}{W_1+W_2}\Big|_{\mathbf{x}_4} + \hat{h}_4 h_3 \frac{W_1}{W_1+W_2+W_3}\Big|_{\mathbf{x}_4} \\
&\quad + \hat{h}_5 h_1 \frac{W_1}{W_1+W_2+W_3}\Big|_{\mathbf{x}_5} + \hat{h}_6(h_1+h_3)\frac{W_1}{W_1+W_3}\Big|_{\mathbf{x}_6} \\
&\quad + \hat{h}_6 h_2 \frac{W_1}{W_1+W_2+W_3}\Big|_{\mathbf{x}_6}, \\
f_2 &= \hat{h}_2 + \hat{h}_4(h_1+h_2)\frac{W_2}{W_1+W_2}\Big|_{\mathbf{x}_4} + \hat{h}_4 h_3 \frac{W_2}{W_1+W_2+W_3}\Big|_{\mathbf{x}_4} \\
&\quad + \hat{h}_5(h_2+h_3)\frac{W_2}{W_2+W_3}\Big|_{\mathbf{x}_5} + \hat{h}_5 h_1 \frac{W_2}{W_1+W_2+W_3}\Big|_{\mathbf{x}_5} \\
&\quad + \hat{h}_6 h_2 \frac{W_2}{W_1+W_2+W_3}\Big|_{\mathbf{x}_6}, \\
f_3 &= \hat{h}_3 + \hat{h}_4 h_3 \frac{W_3}{W_1+W_2+W_3}\Big|_{\mathbf{x}_4} + \hat{h}_5(h_2+h_3)\frac{W_3}{W_2+W_3}\Big|_{\mathbf{x}_5} \\
&\quad + \hat{h}_5 h_1 \frac{W_3}{W_1+W_2+W_3}\Big|_{\mathbf{x}_5} + \hat{h}_6(h_1+h_3)\frac{W_3}{W_1+W_3}\Big|_{\mathbf{x}_6} \\
&\quad + \hat{h}_6 h_2 \frac{W_3}{W_1+W_2+W_3}\Big|_{\mathbf{x}_6}
\end{aligned} \tag{1.3}$$

where in the natural coordinate system r,s,

$$\begin{aligned}
h_1 &= 1 - r - s, \\
h_2 &= r, \\
h_3 &= s
\end{aligned} \tag{1.4}$$

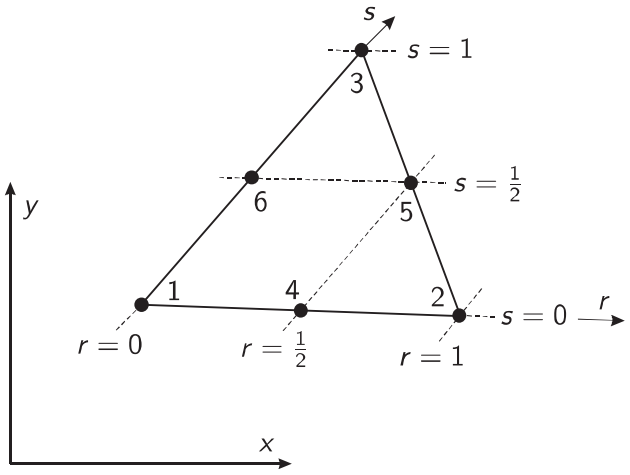

Fig. A1. Coordinate system and nodal points for triangular element.

and

$$\begin{aligned}
\hat{h}_4 &= 4r(1-r-s), \\
\hat{h}_5 &= 4rs, \\
\hat{h}_6 &= 4s(1-r-s), \\
\hat{h}_1 &= 1 - r - s - \frac{1}{2}(\hat{h}_4 + \hat{h}_6), \\
\hat{h}_2 &= r - \frac{1}{2}(\hat{h}_4 + \hat{h}_5), \\
\hat{h}_3 &= s - \frac{1}{2}(\hat{h}_5 + \hat{h}_6)
\end{aligned} \tag{1.5}$$

Note that

$$\sum_{J=1}^{3} f_J = \sum_{i=1}^{6} \hat{h}_i = 1 \tag{1.6}$$

In the form (1.1), the overlapping procedure given in Section 2 is implicit in the functions $f_J, J = 1,2,3$.

If $r_I \to \infty, I = 1,2,3$, we see that $W_I \to 1, I = 1,2,3$, and we have

$$\begin{aligned}
f_1 &= \hat{h}_1 + \hat{h}_4(h_1+h_2)\frac{1}{2} + \hat{h}_4 h_3 \frac{1}{3} + \hat{h}_5 h_1 \frac{1}{3} + \hat{h}_6(h_1+h_3)\frac{1}{2} + \hat{h}_6 h_2 \frac{1}{3} = h_1, \\
f_2 &= \hat{h}_2 + \hat{h}_4(h_1+h_2)\frac{1}{2} + \hat{h}_4 h_3 \frac{1}{3} + \hat{h}_5(h_2+h_3)\frac{1}{2} + \hat{h}_5 h_1 \frac{1}{3} + \hat{h}_6 h_2 \frac{1}{3} = h_2, \\
f_3 &= \hat{h}_3 + \hat{h}_4 h_3 \frac{1}{3} + \hat{h}_5(h_2+h_3)\frac{1}{2} + \hat{h}_5 h_1 \frac{1}{3} + \hat{h}_6(h_1+h_3)\frac{1}{2} + \hat{h}_6 h_2 \frac{1}{3} = h_3
\end{aligned} \tag{1.7}$$

i.e., Eq. (1.1) becomes

$$\mathbf{u} = \sum_{J=1}^{3} h_J \sum_{n \in \mathfrak{I}} p_n \mathbf{a}_{Jn} \tag{1.8}$$

which is the approximation scheme employed in the finite element enriched by interpolation covers.

References

[1] Owen SJ. A survey of unstructured mesh generation technology. In: IMR; 1998. p. 239–67.
[2] Teng SH, Wong CW. Unstructured mesh generation: theory, practice, and perspectives. Int J Comput Geom Appl 2000;10:227–66.
[3] Ito Y. Challenges in unstructured mesh generation for practical and efficient computational fluid dynamics simulations. Comput Fluids 2013;85:47–52.
[4] Steinbrenner JP, Wyman NJ, Chawner JR. Fast surface meshing on imperfect CAD models. In: IMR; 2000. p. 33–41.
[5] Liu GR. Meshfree methods: moving beyond the finite element method. Taylor & Francis; 2009.
[6] De S, Bathe KJ. Towards an efficient meshless computational technique: the method of finite spheres. Eng Comput 2001;18:170–92.
[7] Babuška I, Banerjee U, Osborn JE, Li Q. Quadrature for meshless methods. Int J Numer Meth Eng 2008;76:1434–70.
[8] Babuška I, Banerjee U, Osborn JE, Zhang Q. Effect of numerical integration on meshless methods. Comput Mech Appl Mech Eng 2009;198:2886–97.
[9] Nicomedes WL, Bathe KJ, Moreira FJS, Mesquita RC. Meshfree analysis of electromagnetic wave scattering from conducting targets: formulation and computations. Comput Struct 2017;184:36–52.
[10] Bathe KJ. The finite element method with 'overlapping finite elements'. In: Zingoni A, editor. Proceedings sixth international conference on structural engineering, mechanics and computation – SEMC 2016, Cape Town, South Africa.
[11] Bathe KJ, Zhang L. The finite element method with overlapping elements – a new paradigm for CAD driven simulations. Comput Struct 2017;182:526–39.
[12] Zhang L, Bathe KJ. Overlapping finite elements for a new paradigm of solution. Comput Struct 2017;187:64–76.
[13] Zienkiewicz OC, Taylor RL. The finite element method, vol. 1 & 2. McGraw-Hill; 1989/1990.
[14] Bathe KJ. Finite element procedures. Prentice Hall; 1996; 2nd ed. KJ Bathe, Watertown, MA; 2014; also published by Higher Education Press China; 2016.
[15] Payen DJ, Bathe KJ. A stress improvement procedure. Comput Struct 2012;112:311–26.
[16] Starius G. Composite mesh difference methods for elliptic boundary value problems. Numer Math 1977;28:243–58.
[17] Steger JL, Benek JA. On the use of composite grid schemes in computational aerodynamics. Comput Mech Appl Mech Eng 1987;64:301–20.
[18] Chesshire G, Henshaw WD. Composite overlapping meshes for the solution of partial differential equations. JCP 1990;90:1–64.
[19] Henshaw WD, Petersson NA. A split-step scheme for the incompressible Navier-Stokes equations. Numer Simul Incompressible Flows 2003;2502:108–25.
[20] Henshaw WD. A high-order accurate parallel solver for Maxwell's equations on overlapping grids. SIAM J Sci Comput 2006;28:1730–65.
[21] Kim J, Bathe KJ. The finite element method enriched by interpolation covers. Comput Struct 2013;116:35–49.
[22] Oden JT, Duarte CA, Zienkiewicz OC. A new cloud-based hp finite element method. Comput Methods Appl Mech Eng 1998;153:117–26.
[23] Keast P. Moderate-degree tetrahedral quadrature formulas. Comput Methods Appl Mech Eng 1986;55:339–48.